Understanding the Structural Phase Transitions in $Na_3V_2(PO_4)_3$ Symmetrical Sodium-Ion Batteries Using Synchrotron-Based X-Ray Techniques

*Ranjith Thangavel, Daseul Han, Brindha Moorthy, Bala Krishnan Ganesan, Megala Moorthy, Yongll Park, Kyung-Wan Nam, and Yun-Sung Lee**

Sodium-ion batteries (SIBs) hold great potential for use in large-scale grid storage applications owing to their low energy cost compared to lithium analogs. The symmetrical SIBs employing $Na_3V_2(PO_4)_3$ (NVP) as both the cathode and anode are considered very promising due to negligible volume changes and longer cycle life. However, the structural changes associated with the electrochemical reactions of symmetrical SIBs employing NVP have not been widely studied. Previous studies on symmetrical SIBs employing NVP are believed to undergo one mole of Na^+ storage during the electrochemical reaction. However, in this study, it is shown that there are significant differences during the electrochemical reaction of the symmetrical NVP system. The symmetrical sodium-ion cell undergoes ≈2 moles of Na^+ reaction (intercalation and deintercalation) instead of 1 mole of Na^+. A simultaneous formation of $Na_5V_2(PO_4)_3$ phase in the anode and $NaV_2(PO_4)_3$ phase in the cathode is revealed by synchrotron-based X-ray diffraction and X-ray absorption spectroscopy. A symmetrical NVP cell can deliver a stable capacity of ≈99 mAh g^{-1}, (based on the mass of the cathode) by simultaneously utilizing V^{3+}/V^{2+} redox in anode and V^{3+}/V^{4+} redox in cathode. The current study provides new insights for the development of high-energy symmetrical NIBs for future use.

1. Introduction

With an unprecedented increase in fossil fuel consumption and global warming, there is an increased focus on renewable energy resources such as solar and wind power.[1,2] However, to efficiently handle the intermittent energy from renewable resources, grid energy storage using an electrical energy storage system (ESS) becomes extremely important. Electrochemical energy storage devices such as batteries and capacitors can store electrical energy efficiency in large-scale ESS and deliver it on demand.[3] Substantial research on lithium-ion batteries (LIBs) over the past two decades has made them a prime candidate for electric and hybrid vehicle applications.[4,5] However, LIB technologies are not economically feasible for large-scale ESS applications due to the limited availability of lithium-ion resources and their high cost. SIBs have gained an enormous interest for large-scale ESS applications owing to a similar working chemistry to LIBs, wide availability, and low cost.[6,7]

From the conventional $NaMO_2$ type layered oxide cathode (M = Fe, Ni, Co) to the recent new class of Prussian blue analogs, fluoro-phosphate, and sulfate-based cathodes, considerable progress has been made in NIB cathodes.[8,9] Similarly, anodes based on carbonaceous materials, oxides, metal sulfides, and metals with high capacity and high capability rate have been identified.[10–13] Further, a few companies like Faradion Limited, Tamat, and Novasis Energies have developed a prototype SIB system, and they are on the verge of commercialization.

Owing to thermal stability and sodium plating, the conventional asymmetric type SIBs utilizing carbon/sodium metal anode and the transition metal-containing cathode could trigger issues, thus reducing the cycle life and safety of large-scale ESS devices. The symmetrical SIBs are very promising because of their similar cathode and anode configuration, exhibiting negligible volume changes (the volume shrinkage in cathode will be buffered by the anode expansion and vice versa) during the charge/discharge process and making SIBs highly stable.[14,15] However, symmetrical SIBs are not widely studied due to the absence of bipolar electrodes capable of functioning both as anode and cathode.[16]

R. Thangavel, B. K. Ganesan, M. Moorthy, Y. Park, Y.-S. Lee
School of Chemical Engineering
Chonnam National University
Gwangju 61186, Republic of Korea
E-mail: leeys@chonnam.ac.kr

R. Thangavel
Department of Energy Science
Sungkyunkwan University
Suwon 16419, Republic of Korea

R. Thangavel
The Institute of New Paradigm of Energy Science Convergence
Sungkyunkwan University
Suwon 16419, Republic of Korea

D. Han, K.-W. Nam
Department of Energy and Materials Engineering
Dongguk University
Seoul 04620, Republic of Korea

B. Moorthy
Department of Materials Science and Engineering
Korea Advanced Institute of Science and Technology (KAIST)
Daejeon 305-701, Republic of Korea

The ORCID identification number(s) for the author(s) of this article can be found under https://doi.org/10.1002/smtd.202100888.

DOI: 10.1002/smtd.202100888

Several NASICON (sodium superionic conductor) based $Na_xM(PO_4)_3$ (M = V, Ti, Mn, Cr, Fe, etc.) have high potential to function efficiently as bipolar electrodes due to multi-redox reactions involving more than two electrons in anodic and cathodic regions.[16–19] Recently, NASICON electrodes have been investigated for their fast ionic diffusion coefficient, lower sodium ion migration barrier than their lithium analog, and excellent sodium-storage performance.[20,21] The interest in polyanionic-based materials for NIBs has increased considerably as they have stable sites for Na ion accommodation with high reversibility and no/negligible volume change.[22] The heavy polyanionic framework provided by the P–O covalent bond establishes excellent chemical and structural stability along with reasonable discharge capacity. Moreover, enhancing their safety could enable their usage in large-scale power grid applications.

Such bifunctional activity has been demonstrated in several electrodes such as $Na_3V_2(PO_4)_3$, $Na_2VTi(PO_4)_3$, $Na_3V_{1.5}Cr_{0.5}(PO_4)_3$, $Na_3MnTi(PO_4)_3$, $Na_3FeV(PO_4)_3$, and $Na_2CrTi(PO_4)_3$.[16–19] Among them, $Na_3V_2(PO_4)_3$ (NVP) has great appeal for symmetrical SIB systems. Flat voltage plateaus, multiredox with a single transition metal, and a large voltage difference between the plateaus of the anodic and cathodic region can greatly improve the output of the NVP symmetrical cell. NVP can undergo redox reactions as a cathode at 3.4 V versus Na/Na^+ for V^{3+}/V^{4+} to reversibly extract $2Na^+$ ions, delivering an energy density of ≈400 Wh kg^{-1}.[23] Similarly, NVP was shown to exhibit a well-defined flat plateau at ≈1.56 V versus Na/Na^+ in the anodic region, indicating the sodium insertion into NVP structure.[24] The reaction mechanism involves the insertion of ≈1 Na^+ into the NVP structure to form $Na_4V_2(PO_4)_3$ through $V^{3+}/V^{2.5+}$ redox, delivering a capacity of ≈55 mAh g^{-1}.[25] The symmetrical SIBs studied with cathodic (3.4 V) and anodic voltage plateaus (1.56 V) showed an output voltage of 1.7 V.

Recently, a new low-voltage behavior of NVP in the anodic region was revealed by Ji and co-workers, which was attributed to the extra insertion of Na-ion into the NVP structure.[26] A new voltage plateau in the NVP at 0.3 V versus Na/Na^+ corresponds to the formation of $Na_5V_2(PO_4)_3$ phase from $Na_4V_2(PO_4)_3$ phase through $V^{2.5+}/V^{2+}$ redox. The insertion of two Na^+ ions in the anodic region of NVP is highly reversible, delivering a stable capacity of ≈150 mAh g^{-1}. However, the phase transitions in symmetrical sodium-ion batteries, employing two Na^+ extractions/insertions in a $Na_3V_2(PO_4)_3$ bipolar electrode, are not understood clearly. In this study, we investigate the electrochemical reactions of the symmetric SIBs with NVP as both cathode and anode by combining $V^{3+}/^{4+}$ cathodic redox couples and $V^{3+}/^{2+}$ anodic redox couple. The structural changes of NVP symmetrical cells, based on synchrotron-based XRD, reveal the ≈$2Na^+$ ion storage by the simultaneous formation of $Na_5V_2(PO_4)_3$ phase in the anode, and $NaV_2(PO_4)_3$ phase in the cathode. Moreover, the charge storage mechanism involving the $2Na^+$ ion in symmetrical NVP is highly reversible. The current study provides new insights for the development of high energy symmetrical sodium ion energy storage devices for future use and warrants structural behavior studies in symmetrical SIB systems.

2. Physical Characterization

The Rigaku Rint 1000, Japan (Cu Kα radiation source) was used to record the XRD patterns of NVP, and the diffraction patterns were refined using Rietveld refinement via FULLPROF software. The backgrounds of the XRD patterns were treated and removed by linear interpolation between selected points, while pseudo-Voigt profile functions were used to fit the diffraction peaks. The morphology of all the samples was studied using a scanning electron microscope (FE-SEM, S4700, Hitachi, Japan) and a transmission electron microscope (TEM, TECNAI, Philips, Netherlands 200 keV). Multilab instrument (monochromatic Al Kα radiation $h\gamma$ = 1486.6 eV) was used for X-ray photoelectron spectroscopy (XPS) analysis. In situ XRD patterns of NVP half-cell, and NVP symmetric cell were collected at 6D-UNIST beamline of Pohang Accelerator Laboratory (PAL) in a transmission mode using an X-ray wavelength = 0.653 Å. The 2θ angles of the XRD patterns displayed in the manuscript were plotted after recalculation based on conventional Cu Kα radiation (λ = 1.54 Å). X-ray absorption spectroscopy (XAS) spectra were measured at 8C beamline of PAL using a Si(111) double crystal monochromator. Ex situ electrode samples with various (dis)charge states were extracted from the NVP symmetrical cells, which were charged and discharged at predetermined cutoff voltages. The electrodes were then sealed with Kapton tape in an Ar-filled glove box to prevent air exposure. V K-edge XAS of these electrode samples were measured in transmission mode. The metallic V reference foil spectrum was also measured simultaneously to calibrate the energy position (E_0 for V foil = 5464 eV).

3. Electrochemical Characterization

The electrochemical performance of NVP was measured in standard CR2032 coin-cell configuration using metallic sodium foil as the counter electrode. The following electrode composition was used: 80% active material, 10% conductive additive (Super P), and 10% binder (PVDF). All the components were mixed and dispersed using N-methyl-2-pyrrolidone solvent and the slurry was pressed over a stainless steel foil. This electrode was then dried at 120 °C for 12 h in a vacuum and used directly for the electrochemical studies. Porous polypropylene (Celgard 3401, USA) film was filled with 1 M $NaClO_4$ in ethylene carbonate/diethyl carbonate (1:1 vol). A Won-A-Tech Battery tester (WBCS 3000, Korea) was used for galvanostatic studies, and the cyclic voltammetry (CV) was analyzed with a Bio-Logic electrochemical work station (SP-150), France.

4. Results and Discussion

The powder XRD patterns and the Rietveld refinement of as-synthesized C-NVP, shown in **Figure 1**, depict the formation of the product phase pure NVP with no impurities. The diffraction peaks of NVP can be well indexed with the NASICON structure with *R*-3*c* space group of hexagonal symmetry.[27] The profile *R*-factor (R_p), and the goodness of fit (chi^2)

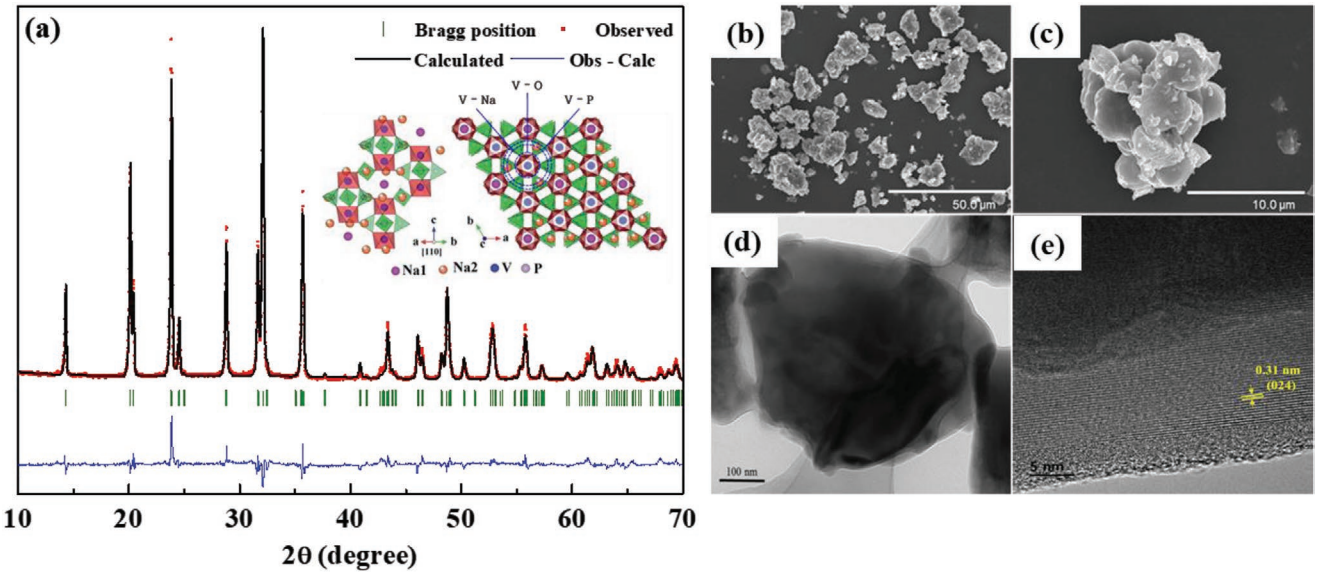

Figure 1. a) Rietveld refinement of the powder XRD diffraction data of NVP, Inset: crystal structure of NVP. b,c) SEM images of NVP. d,e) TEM images of NVP.

reliability factor for Rietveld refinement of the NASICON phase were determined to be ≈8.99 and 9.14 respectively. The calculated lattice parameters, a = 8.7128 Å and c = 21.7756 Å are consistent with previous reports, and have estimated standard deviation of 0.000242 and 0.000911, respectively. The intense diffraction peaks indicate the high crystallinity of the NVP particles and the features of crystalline carbon are not observed in the XRD pattern. The crystal structure of NVP in Figure 1 inset shows the 3D $V_2(PO_4)_3$ framework formed by octahedral VO_6 with tetrahedral PO_4. The NVP crystal structure contains two isolated and partly occupied Na ion site with two different oxygen environments, namely, Na1 site (sixfold coordination) and Na2 site (eightfold coordination). For the $Na_3V_2(PO_4)_3$ crystal unit, one Na ion is occupied at the Na1 site (1.0 occupancy) and two Na ions are occupied at the Na2 site (0.67 occupancy).[20,21] The large interstitial space formed by corner-sharing of octahedral VO_6 and tetrahedral PO_4 can create open 3D framework that provide wider channels than other intercalation compounds, leading to a fast sodium ion diffusion in NVP.[28]

The surface morphology by SEM in Figure 1b,c shows the large micron-sized secondary particles (10 μm) formed by a large number of nanosized primary particles, agglomerated due to high-temperature treatment. The TEM images in Figure 1d,e clearly confirm the presence of a thin and uniform carbon layer over the NVP particles. The HR-TEM images clearly show the lattice fringes, indicating that the NVP particles are highly crystalline in nature, and the lattice fringes have the d-spacing of 0.31 nm which corresponds to (024) lattice planes of NASICON-type NVP. The carbon layer over the NVP particles will greatly improve the electronic conductivity of the NVP particles and is essential for improving the kinetics of the NVP electrode.[29,30] The amount of carbon in NVP was found to be ≈2 wt% by thermogravimetric analysis. The other qualitative and quantitative properties of NVP used in this study can be obtained from our previous report.

5. Anodic Performance

The cyclic voltammetry (CV) profiles of NVP (**Figure 2**a) were collected at a scan rate of 0.1 mV s^{-1} between a voltage range of 0.1–3 V versus Na/Na^+. During the cathodic scan, two redox peaks at around ≈1.6 V and ≈0.3 V versus Na/Na^+. The first redox peak at ≈1.6 V is previously studied and results from the formation of $Na_4V_2(PO_4)_3$ due to sodiation of partially filled 18e sites.[31] The second redox peak at ≈0.3 V is a new redox peak, resulting from the insertion of the second sodium ion into the NVP structure during the transforming from $Na_4V_2(PO_4)_3$ phase to $Na_5V_2(PO_4)_3$ phase.[26] During the consecutive anodic scan, the redox peak at 0.3 V corresponds to the removal of one Na^+ ion to form $Na_5V_2(PO_4)_3$ phase from $Na_4V_2(PO_4)_3$ phase, and the redox peak at 1.5 V indicates the reversal of original $Na_3V_2(PO_4)_3$ phase from $Na_4V_2(PO_4)_3$ after the second Na^+ ion is removed.[24]

Figure 2b shows the galvanostatic charge–discharge profile of NVP in the anodic region between 3.0 and 0.1 V versus Na/Na^+ at a current density of 25 mAh g^{-1}. A capacity of ≈180 mAh g^{-1} was achieved during the first sodiation process, and a reversible capacity of ≈155 mAh g^{-1} was obtained after the consecutive desodiation process, indicating a first cycle coulombic efficiency of 91%. During the discharge process, two plateaus are observed at 1.4 and 0.3 V versus Na/Na^+, and the results are in correlation with the CV studies. The first sodium is inserted into NVP at 1.4 V through $V^{3+}/V^{2.5+}$ redox to form $Na_4V_2(PO_4)_3$ phase, and the second sodium is inserted at 0.3 V through $V^{2.5+}/V^{2+}$ redox to form $Na_5V_2(PO_4)_3$.

The initial discharge capacity of the NVP is higher than the theoretical capacity for the insertion of two Na ions owing to capacity contribution from the carbon additives and electrolyte decomposition.[32] The discharge capacity associated with the first and second sodiation plateau regions corresponds to the insertion of one sodium ion in each region. These results suggest the sequential insertion of two sodium ions into NVP

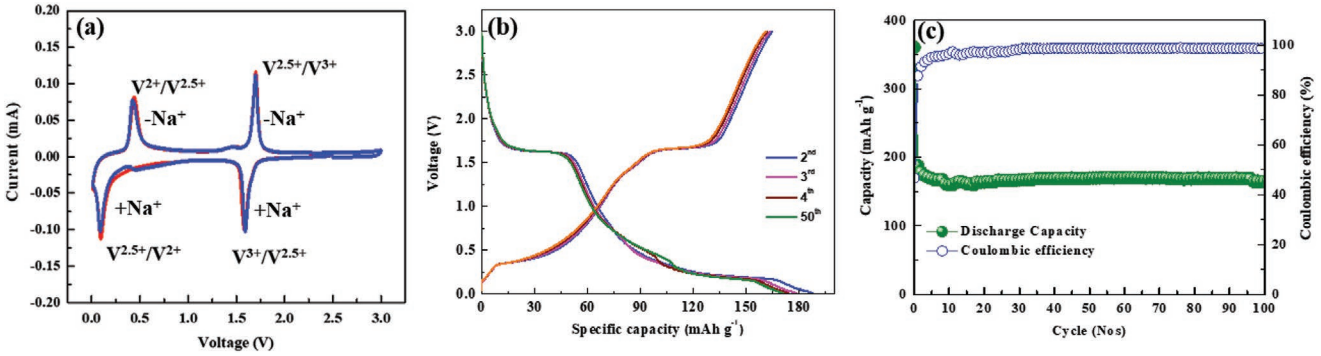

Figure 2. Anodic performance of NVP: a) Cyclic voltammetry curves at 0.1 mV s^{-1}, b) charge/discharge profile at 0.25 A g^{-1}, and c) cyclic stability at 0.25 A g^{-1}.

structure to form $Na_5V_2(PO_4)_3$. The cyclic performance of NVP in Figure 2c depicts the high reversibility of the insertion process of two sodium ions in the NVP anode. After the initial 50 cycles, a discharge capacity of ≈160 mAh g^{-1}, 90% retention, and a high coulombic efficiency is well maintained. The charge/discharge profile of NVP anode at different cycles clearly shows the continuous presence of two plateaus in anodic region without change, indicating the reversibility of the two sodium ion insertion process.

The structural and phase changes during the sodiation reaction of NVP were investigated using the operando synchrotron XRD analysis. **Figure 3** shows the 2θ major regions of the XRD pattern that clearly reflect the structural change in the NVP anode during the sodiation process. During the sodiation process, the XRD peaks do not shift continuously, but they do show a gradual transformation into a more sodiated phase.[33] A gradual drop in peak intensities of the NVP phase along with the gradual emergence of new peaks in the plateau region indicates the sequential formation of $Na_4V_2(PO_4)_3$ and $Na_5V_2(PO_4)_3$ through two-phase reaction.[34] During the following charge process, the diffraction peaks of $Na_5V_2(PO_4)_3$ phase decrease in intensity and disappear eventually due to complete removal of Na^+ ions in a two-phase reaction; meanwhile the reflections of $Na_3V_2(PO_4)_3$ phase appear again, confirming the two-phase desodiation process. This indicates the reversible extraction and insertion process of two Na^+ ions in NVP anode. Figure S3 (Supporting Information) shows the lattice and volume changes during the charge-discharge process of NVP. In $Na_3V_2(PO_4)_3$ crystal structure, two Na ions occupy 18e sites, and one Na ion occupies 6b site. During sodiation, the first sodium ion is inserted into the empty sites of Na2 (18e) site, and the second sodium ion is inserted into the vacant Na3 (6a) site. Thus, the $V_2(PO_4)_3$ framework can accommodate five Na^+ ions to form $Na_5V_2(PO_4)_3$ phase.

6. Cathodic Performance

The Na-ion storage performance of NVP in the cathodic region is evaluated between 2.5 and 3.8 V versus Na/Na^+ at a rate of 0.5 C. The charge profile of NVP in **Figure 4**a shows a flat plateau at ≈3.4 V due to sodium ion extraction through V^{3+}/V^{4+} redox reaction and the corresponding phase transformation from $Na_3V_2(PO_4)_3$ to $NaV_2(PO_4)_3$.[35] During sodium ion extraction from $Na_3V_2(PO_4)_3$, two Na^+ ions from Na2-site are removed completely, whereas one Na ion in Na1 site remains. The re-insertion of sodium ion occurs through V^{4+}/V^{3+} redox reaction, and the reversal of $Na_3V_2(PO_4)_3$ phase occurs.[36] In the cathodic region, the NVP can deliver a capacity of ≈103 mAh g^{-1} at 0.5 C with low polarization, and the capacity loss is nearly negligible even after 100 cycles (Figure 4b). Furthermore, the NVP cathode delivered a discharge capacity of 100, 94, 90, 85 mAh g^{-1} at 1 C, 2.5 C, 5 C, 10 C, respectively (Figure S1, Supporting Information).

7. Symmetrical Cell

Based on the above results, symmetric sodium-ion cells were assembled using fresh NVP electrodes as both the anode and cathode. Considering 2 Na^+ ion storage in the anode and 2 Na^+ ion extraction in the cathode, the mass ratio between the anode and cathode is controlled to be 1: 1. The charge-discharge profile (**Figure 5**) of symmetrical NVP delivers a capacity of ≈99 mAh g^{-1} at 0.1C, nearly equivalent to the reaction involving 2Na^+ ion. By nanostructuring (nanowires, nanorods, nanospheres etc.,) the NVP particles or by using highly conductive carbon network (graphene/CNT), the low capacity of NVP, caused by kinetic issues in low electronic conductivity, can be improved.[37] The first cycle coulombic efficiency is ≈81%, which can be improved by optimizing the electrolyte composition.

To obtain further insights on the storage mechanism of the NVP symmetrical cell, in-situ XRD measurements were carried out during the charge–discharge process. **Figure 6** shows the major 2θ regions of NVP centered at 23.8°, 28.8°, and 32.1°, corresponding to the (113), (024), and (116) lattice planes of $Na_3V_2(PO_4)_3$, that can well reflect the structural changes in the NVP during the electrochemical reaction. Before the charge process, the diffraction patterns of both the anode and cathode are identified as the $Na_3V_2(PO_4)_3$ phase. Upon charging, the XRD peaks in the cathode side shrink gradually and new peaks progressively emerge on the right side of the original state, indicating the removal of sodium ions from the cathode. At the end of the charge process, the peaks of $Na_3V_2(PO_4)_3$ phase completely disappear and new diffraction peaks corresponding to $NaV_2(PO_4)_3$ emerge.[38] Meanwhile, an opposite trend is observed on the anode side of the NVP during the charge process. The diffraction peaks of NVP anode shift

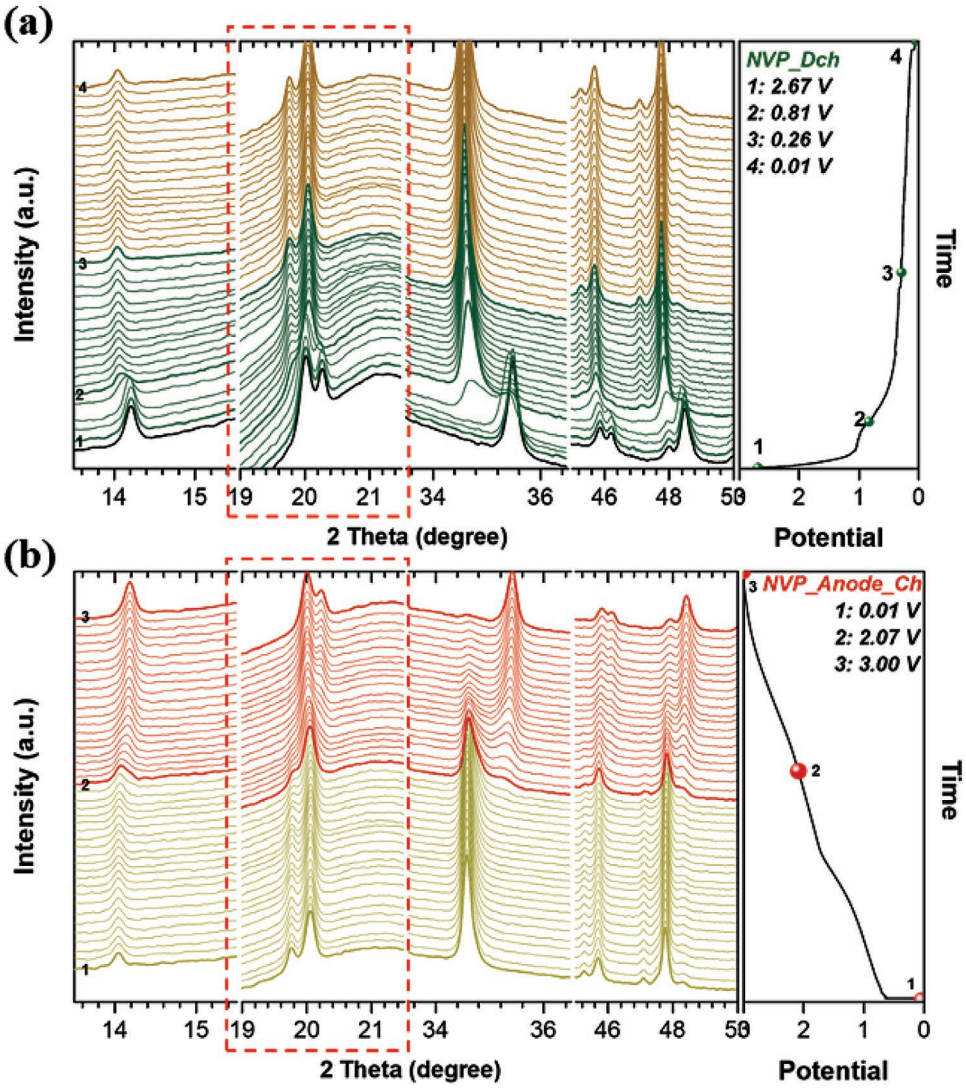

Figure 3. Operando XRD patterns with the electrochemical voltage–capacity curve of NVP in the voltage range of 3.0 to 0.01 V a) discharge and b) charge.

gradually to smaller angles, indicating the simultaneous insertion of sodium ions into the NVP anode. Upon full charging, the peaks of (001) planes of $Na_3V_2(PO_4)_3$ disappear completely and new peaks at ≈20.5 can be well indexed to $Na_5V_2(PO_4)_3$.[39] The reversal of the above process occurs during the consecutive discharge process. The diffraction patterns of $NaV_2(PO_4)_3$ at ≈24.2° shifts back to smaller angles, indicating the reinsertion of Na ions into $NaV_2(PO_4)_3$ to form $Na_3V_2(PO_4)_3$. Similarly, the diffraction patterns of $Na_5V_2(PO_4)_3$ phase undergo facile transition and completely revert to $Na_3V_2(PO_4)_3$ by giving $2Na^+$ ions to the cathode. The $Na_3V_2(PO_4)_3$ phase reemerge after the discharge process indicating the high reversibility of two sodium-ion extraction in the cathode and sodium ion insertion process in the anode.

The schematic diagram of the working mechanism of the symmetric NVP full cell is depicted in **Figure 7**. The $Na_3V_2(PO_4)_3$ phase contains three sodium-ion storage site: i) Na1 (6b) site with 1 Na occupancy, ii) Na2 (18e) site with 2Na occupancy, and iii) Na3 site with no Na occupancy. During the initial charging process, one Na^+ from the Na2 site of the cathode is removed and stored at the Na2 site of the anode. During this step, $Na_2V_2(PO_4)_3$ phase is formed in the cathode, and $Na_4V_2(PO_4)_3$ phase is formed in the anode. Upon continuous charging, the second Na^+ from the Na1 site of the cathode is removed and stored at the empty Na3 site of the anode. The final phase of the cathode and anode after the charge step is $NaV_2(PO_4)_3$ and $Na_5V_2(PO_4)_3$ respectively. Upon discharge, the Na-ions from the Na3 and Na2 sites of the anode deintercalated and were stored back at the Na1 and Na2 sites of the cathode.[26,31] Both anode and cathode return to $Na_3V_2(PO_4)_3$ phase after the discharge process.

Figure 8 and Table S1 (Supporting Information) show the lattice parameter and volume changes in the symmetrical NVP cell at different state of the charge and discharge during the charge-discharge process. The lattice parameters are obtained by refinement of in situ XRD curves of symmetrical NVP at different state of charge and discharge. The refinement curves are given in Figure S2 (Supporting Information). During the charge

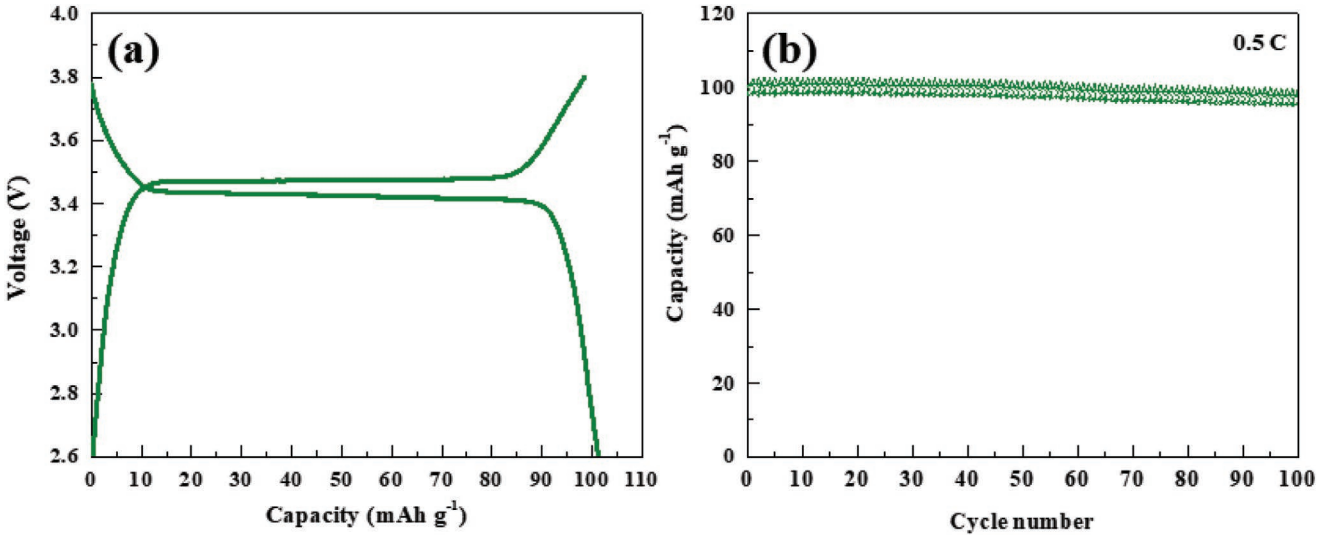

Figure 4. Cathodic performance of NVP: a) Charge/discharge profile at 0.5 C and b) cyclic stability at 0. 5 C.

process, the "*a*" lattice parameter of the NVP cathode gradually decreases due to the removal of Na-ions from the lattice structure. Generally, the lattice parameter values of NVP cathode get decreased during Na-ion removal due to the removal of the sodium steric effect. As the desodiation proceeds, the lattice parameters shrink and new peaks corresponding to the desodiated phase -$NaV_2(PO_4)_3$ appear at a higher angle due to a two-phase desodiation process. A simultaneous increase in the "*a*" lattice parameter of the NVP anode is noted due to the insertion of Na ions into the NVP crystal lattice. The lattice changes in NVP anode are mainly attributed to the two-phase sodium-ion insertion into NVP structure that increases the sodium cation repulsion, and reduce the anion repulsions in tetrahedral PO_4. Meanwhile, the "*c*" lattice parameter decreases for both the cathode and anode during the charge process due to electrostatic repulsion in NVP unit cell after Na ion extraction/insertion.[40] The "*a*" and "*c*" lattice parameters of the NVP cathode after the charge process is a = 8.3943(3) Å and c = 21.4283(11) Å which corresponds to $NaV_2(PO_4)_3$. This indicates the complete transformation of $Na_3V_2(PO_4)_3$ phase to $NaV_2(PO_4)_3$ after the end of the charge process. Similarly, the "*a,*" and "*c*" lattice parameters of the NVP anode after charge process is a = 8.9319(2) Å and c = 21.4171(9) Å, which corresponds to $Na_5V_2(PO_4)_3$.[31] The lattice parameter values are much closer to the lattice parameter values obtained from half-cell anodic performance.

The lattice parameters of both the NVP anode and cathode in the symmetrical cell revert to the original values after the discharge process, indicating the highly reversible nature of the electrochemical reaction. The lattice changes are attributed to the reoccurrence of sodium steric effect during phase transition from $NaV_2(PO_4)_3$ to $Na_3V_2(PO_4)_3$ phase (cathode), and reduction in anionic repulsions due to sodium ion removal during phase transition from $Na_5V_2(PO_4)_3$ to $Na_3V_2(PO_4)_3$ phase (anode). The "*a*" and "*c*" lattice parameters of the NVP cathode after the discharge process are a = 8.6754(5) Å and c = 21.6913(17) Å,

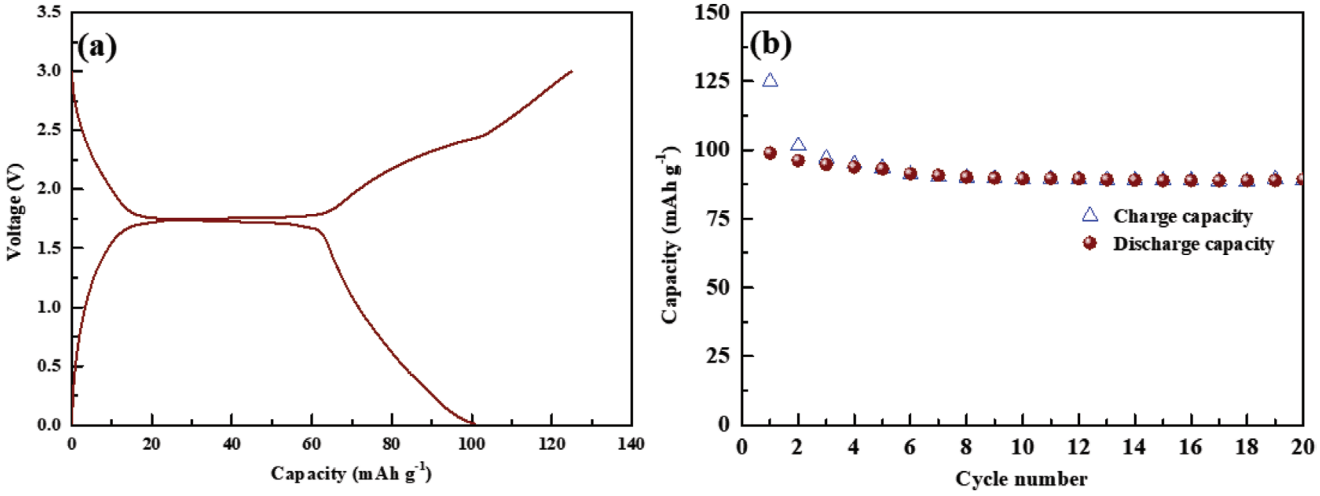

Figure 5. Performance of symmetrical NVP cells: a) Charge/discharge profile at 0.1 C and b) cyclic stability at 0. 1 C.

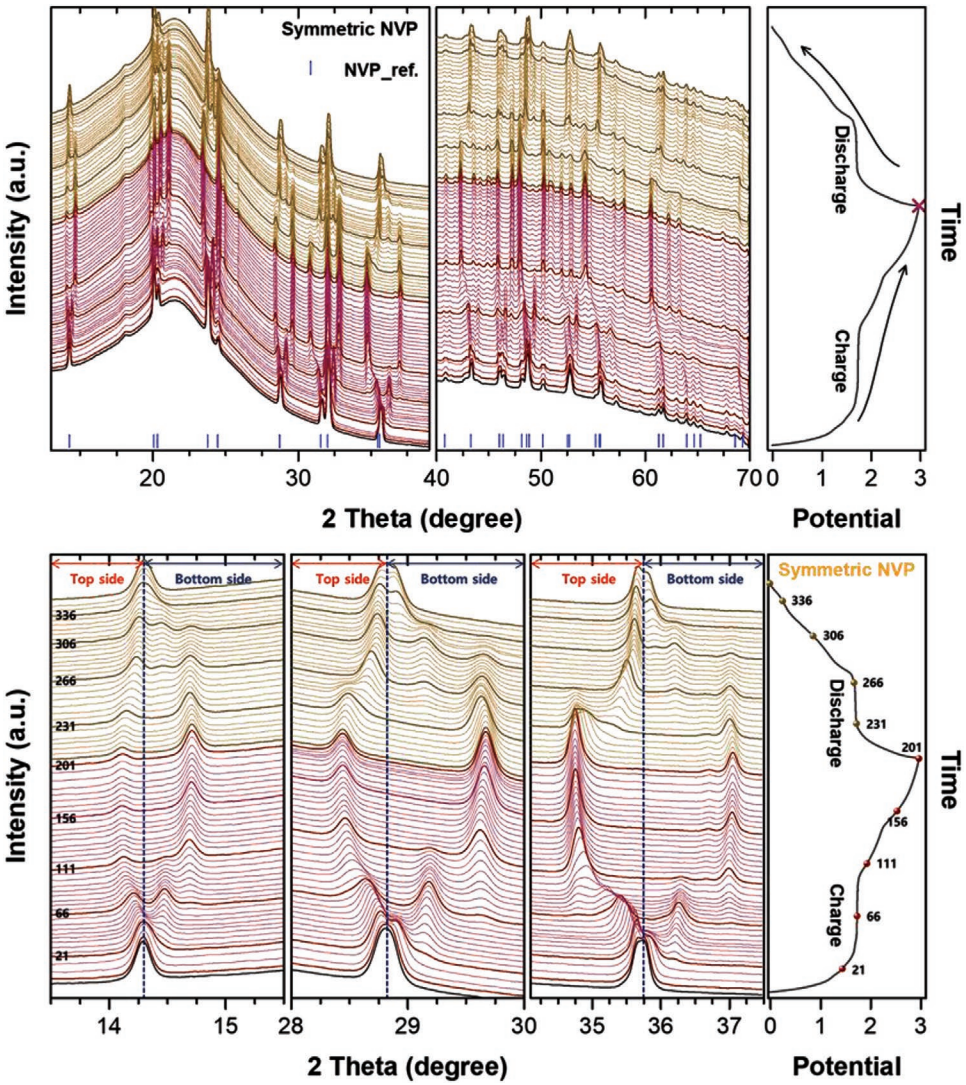

Figure 6. Operando XRD patterns of symmetrical NVP cell with the electrochemical voltage curve of NVP in the voltage range of 3.0 to 0.01 V.

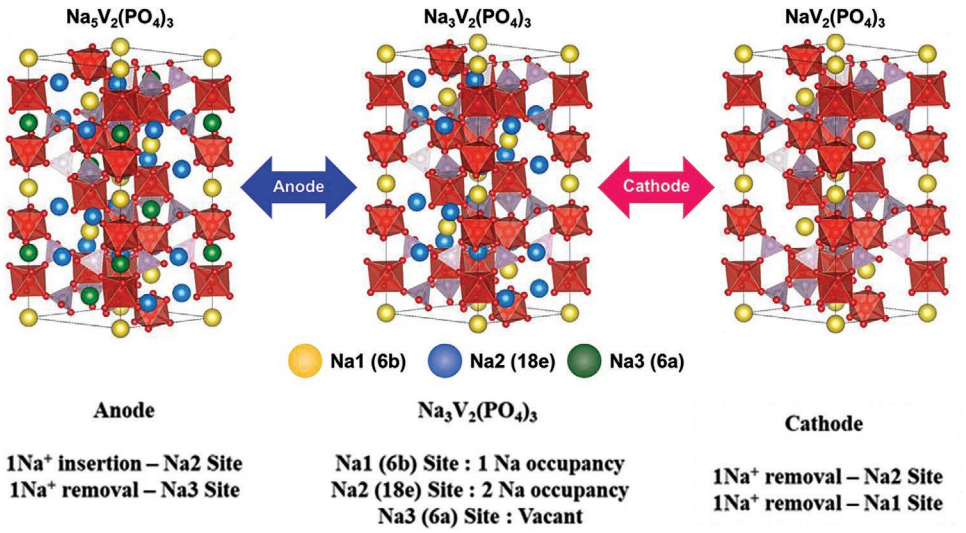

Figure 7. Scheme on working mechanism of symmetrical NVP.

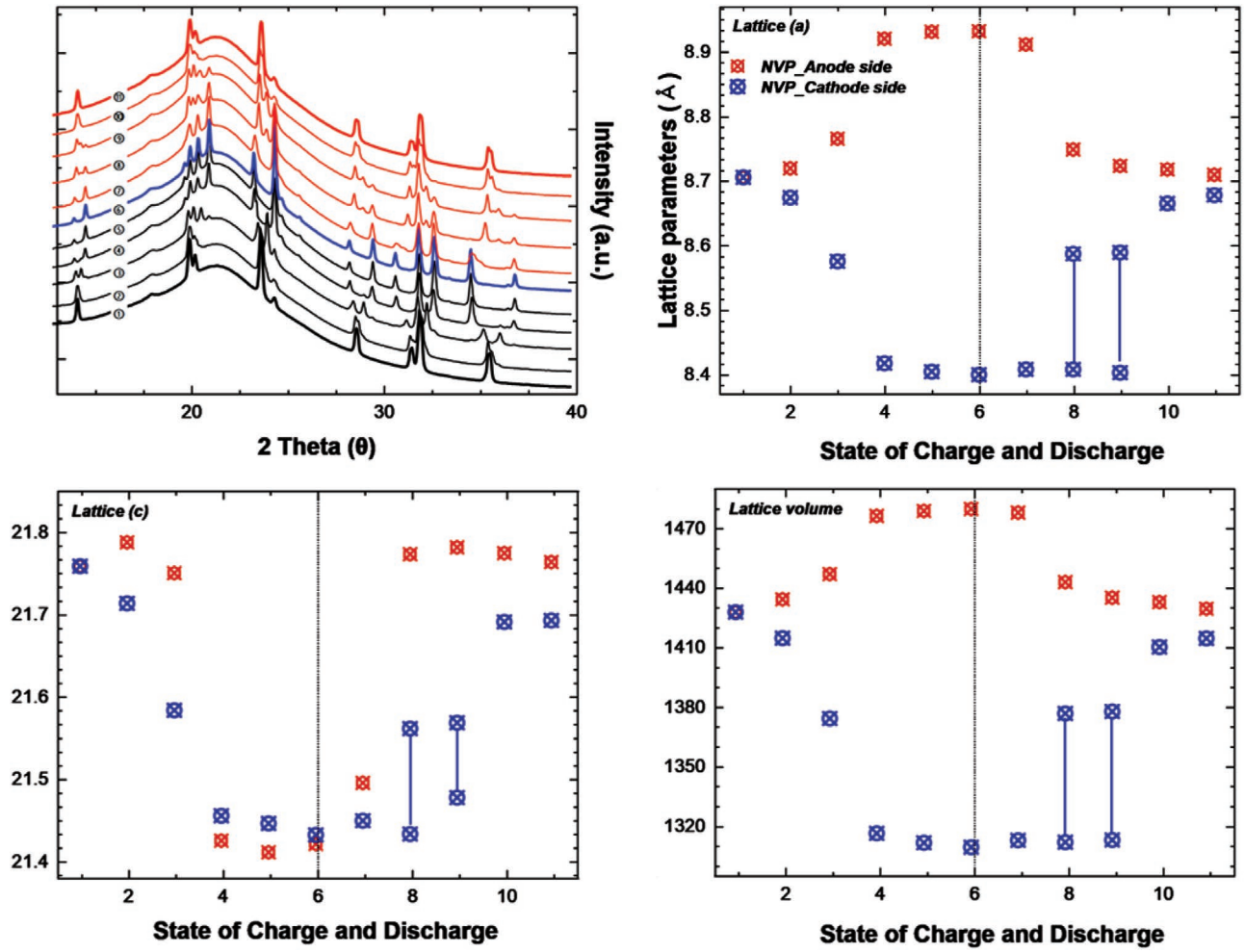

Figure 8. Lattice parameters (*a*, *b*, *c*) and unit cell volume (*V*) in symmetrical NVP cell during first cycle.

respectively, while the "*a*" and "*c*" lattice parameters of the NVP anode after discharge process are *a = 8.7071(3) Å* and *c = 21.7629(10) Å*, respectively. The values are much closer to the pristine $Na_3V_2(PO_4)_3$ state. The slight irreversibility is attributed to the initial formation of SEI layer and electrolyte decomposition during the first cycle, which was previously noted with first cycle coulombic efficiency of ≈81% in the symmetrical cells. A volume expansion of ≈9% is noted for the NVP cathode during the charge process, and the volume expansion is countered by simultaneous volume shrinkage (10%) in the NVP anode. Such small volume expansion in the cathode and simultaneous volume shrinkage in the anode to counter the change is favorable for maintaining the structural integrity of the SIB system and improving the electrochemical performance.

The oxidation states of vanadium ion in NVP electrodes during charge/discharge are inferred through V K-edge XAS and the corresponding spectra are given in Figure S3 (Supporting Information). When compared with the standard spectra of V^{3+} (i.e., V_2O_3) and V^{4+} (i.e., V_2O_4) reference compounds, the average oxidation state of vanadium in the pristine NVP electrode was close to V^{3+}.[41] During charging, a significant shift toward higher absorption energy was observed for the NVP cathode. The oxidation state of fully charged NVP cathode is close to V^{4+}, confirming the removal of ≈$2Na^+$ ions from the cathode.[42] Additionally, the characteristic pre-edge spectrum of V^{3+} at 5469 eV shifts to ≈5471 eV, indicating the tetravalent state of vanadium in NVP cathode.[43] Meanwhile, we speculate the lower oxidation state of V^{2+} is not stable such that ex situ XAS measurement for NVP anode is not able to capture V^{2+} state. The metastability of V^{2+} phase is due to thermodynamic instability with being easily oxidized, which was reported in various energy systems.[44,45] Also, a previous report revealed that the $Na_5V_2(PO_4)_3$ phase is energetically unfavorable due to the high Coulombic repulsion for Na insertion.[26] Upon discharge, the pre-edge and main absorption edge spectra of the cathode shifted back to its initial position, reconfirming the trivalent state (V^{3+}) of vanadium in NVP cathode, and the reversibility of storage mechanism.

Furthermore, ex situ XPS studies were carried out to examine the Na extraction/insertion in NVP symmetrical cell (Figure S4, Supporting Information). The V2p XPS spectrum has binding energy value of ≈516 eV, which corresponds to V 2p3/2 orbital, indicating the trivalent state (V^{3+}) of the vanadium in NVP.[46] The transition from $Na_3V_2(PO_4)_3$ phase to $NaV_2(PO_4)_3$ in NVP

cathode is accompanied by the V^{3+} to V^{4+} redox, and the transition from $Na_3V_2(PO_4)_3$ phase to $Na_5V_2(PO_4)_3$ is accompanied by V^{3+} to V^{2+} redox.[25,47] After charge, the binding energy of V2p XPS spectrum in the NVP cathode increased significantly to 517 eV, indicating the formation of a higher oxidation state (V^{4+}).[25,48] Meanwhile, binding energy of V2p XPS spectrum in the NVP anode was reduced to 514 eV, indicating the reduction in the oxidation state of NVP due to the insertion of Na^+ ions. In this state, a combination of V^{2+} and V^{3+} is detected due to highly unstable nature of V^{2+} in the ambient atmosphere.[49] The above results show the intercalation and de-intercalation of two Na^+ ions in the NVP symmetrical cell.

8. Conclusion

In summary, the charge storage mechanism and structural changes associated with the electrochemical reaction in symmetrical SIBs, employing $Na_3V_2(PO_4)_3$ as both the anode and cathode, has been systematically investigated using operando synchrotron XRD techniques. The symmetrical NVP cells can reversibly intercalate/de-intercalate ≈2 moles of Na ions (≈99 mAh g^{-1}) instead of 1 mole of Li (≈50 mAh g^{-1}). The charge storage process in NVP symmetrical SIBs involves the simultaneous formation of $NaV_2(PO_4)_3$ phase through V^{3+}/V^{4+} redox in the cathode, and $Na_5V_2(PO_4)_3$ phase through V^{3+}/V^{2+} redox in the anode, by accommodating the Na-ions from the cathode. More importantly, the two-sodium-based charge storage mechanism in the NVP symmetrical cell is highly reversible, delivering a stable electrochemical performance upon cycling. These findings not only provide new understanding on sodium-ion storage mechanism in symmetrical NVP cells, but also warrant the investigation of charge storage mechanism in symmetrical cells employing other bi-functional electrodes.

9. Experimental Section

The synthesis procedure for NVP–carbon was adapted from our previous work.[46] The NVP–carbon composite electrode was synthesized by the sol–gel method by using V_2O_5, $NH_4H_2PO_4$, and Na_2CO_3 as precursors. Oxalic acid and ethylene glycol were used as the reducing agent and carbon source, respectively. A stoichiometric amount of V_2O_5 and oxalic acid was dissolved at 100 °C in water, followed by the other precursors. The gel formed was ground, pelletized, and heated at 350 °C for 3 h in an Ar/H_2 atmosphere. It was then regrounded, pelletized, and heat-treated again at 700 °C for 8 h in an Ar/H_2 atmosphere.

Supporting Information

Supporting Information is available from the Wiley Online Library or from the author.

Acknowledgements

This work was supported by the National Research Foundation of Korea (NRF) grant funded by the Korea government (Ministry of Science, ICT & Future Planning) (No. 2019R1A4A2001527). R.T. acknowledges the support from National Research Foundation of Korea (NRF) grant funded by the Korea government (MSIT) (No. 2020R1C1C1014961).

Conflict of Interest

The authors declare no conflict of interest.

Data Availability Statement

Research data are not shared.

Keywords

cathodes, NASICON, operando X-ray, sodium-ion batteries, storage mechanisms

Received: August 3, 2021
Revised: November 21, 2021
Published online: December 16, 2021

[1] M. Ben Yahia, J. Vergnet, M. Saubanère, M.-L. Doublet, *Nat. Mater.* **2019**, *18*, 496.
[2] P. K. Nayak, L. Yang, W. Brehm, P. Adelhelm, *Angew. Chem.* **2018**, *57*, 102.
[3] C. Liu, F. Li, L.-P. Ma, H.-M. Cheng, *Adv. Mater.* **2010**, *22*, E28.
[4] N. Yabuuchi, *Chem. Rec.* **2019**, *19*, 690.
[5] W. Lee, S. Muhammad, T. Kim, H. Kim, E. Lee, M. Jeong, S. Son, J.-H. Ryou, W.-S. Yoon, *Adv. Energy Mater.* **2018**, *8*, 1701788.
[6] C. Delmas, *Adv. Energy Mater.* **2018**, *8*, 1703137.
[7] J.-Y. Hwang, S.-T. Myung, Y.-K. Sun, *Chem. Soc. Rev.* **2017**, *46*, 3529.
[8] J. Kim, I. Park, H. Kim, K.-Y. Park, Y.-U. Park, K. Kang, *Adv. Energy Mater.* **2016**, *6*, 1502147.
[9] H. Kim, H. Kim, Z. Ding, M. H. Lee, K. Lim, G. Yoon, K. Kang, *Adv. Energy Mater.* **2016**, *6*, 1600943.
[10] R. Thangavel, A. Samuthira Pandian, H. V. Ramasamy, Y.-S. Lee, *ACS Appl. Mater. Interfaces* **2017**, *9*, 40187.
[11] R. Thangavel, B. Moorthy, D. K. Kim, Y.-S. Lee, *Adv. Energy Mater.* **2017**, *7*, 1602654.
[12] J. M. Lee, G. Singh, W. Cha, S. Kim, J. Yi, S.-J. Hwang, A. Vinu, *ACS Energy Lett.* **2020**, *5*, 1939.
[13] Y. Liang, W.-H. Lai, Z. Miao, S.-L. Chou, *Small* **2018**, *14*, 1702514.
[14] X. Liu, X. Jiang, F. Zhong, X. Feng, W. Chen, X. Ai, H. Yang, Y. Cao, *ACS Appl. Mater. Interfaces* **2019**, *11*, 27833.
[15] Y. Zhou, X. Shao, K.-h. Lam, Y. Zheng, L. Zhao, K. Wang, J. Zhao, F. Chen, X. Hou, *ACS Appl. Mater. Interfaces* **2020**, *12*, 30328.
[16] S. Guo, H. Yu, P. Liu, Y. Ren, T. Zhang, M. Chen, M. Ishida, H. Zhou, *Energy Environ. Sci.* **2015**, *8*, 1237.
[17] H. Gao, J. B. Goodenough, *Angew. Chem.* **2016**, *55*, 12768.
[18] W. Gao, R. Zhan, M. K. Aslam, D. Liu, J. Jiang, M. Xu, *Energy Storage Mater.* **2019**, *1*, e74.
[19] A. Gilankar, A. Mitra, J. Singh, S. Das, S. B. Majumder, *J. Alloys Cmpd.* **2021**, *851*, 156813.
[20] M. Chen, W. Hua, J. Xiao, D. Cortie, W. Chen, E. Wang, Z. Hu, Q. Gu, X. Wang, S. Indris, S.-L. Chou, S.-X. Dou, *Nat. Commun.* **2019**, *10*, 1480.
[21] S. Chen, C. Wu, L. Shen, C. Zhu, Y. Huang, K. Xi, J. Maier, Y. Yu, *Adv. Mater.* **2017**, *29*, 1700431.
[22] C. Masquelier, L. Croguennec, *Chem. Rev.* **2013**, *113*, 6552.
[23] Z. Jian, W. Han, X. Lu, H. Yang, Y.-S. Hu, J. Zhou, Z. Zhou, J. Li, W. Chen, D. Chen, L. Chen, *Adv. Energy Mater.* **2013**, *3*, 156.
[24] D. Wang, N. Chen, M. Li, C. Wang, H. Ehrenberg, X. Bie, Y. Wei, G. Chen, F. Du, *J. Mater. Chem. A* **2015**, *3*, 8636.
[25] K. Saravanan, C. W. Mason, A. Rudola, K. H. Wong, P. Balaya, *Adv. Energy Mater.* **2013**, *3*, 444.

[26] Z. Jian, Y. Sun, X. Ji, *Chem. Commun.* **2015**, *51*, 6381.
[27] H. Li, X. Yu, Y. Bai, F. Wu, C. Wu, L.-Y. Liu, X.-Q. Yang, *J. Mater. Chem. A* **2015**, *3*, 9578.
[28] W. Ren, Z. Zheng, C. Xu, C. Niu, Q. Wei, Q. An, K. Zhao, M. Yan, M. Qin, L. Mai, *Nano Energy* **2016**, *25*, 145.
[29] Z. Lv, M. Ling, H. Yi, H. Zhang, Q. Zheng, X. Li, *ACS Appl. Mater. Interfaces* **2020**, *12*, 13869.
[30] S. Li, Y. Dong, L. Xu, X. Xu, L. He, L. Mai, *Adv. Mater.* **2014**, *26*, 3545.
[31] X. Yao, Z. Zhu, Q. Li, X. Wang, X. Xu, J. Meng, W. Ren, X. Zhang, Y. Huang, L. Mai, *ACS Appl. Mater. Interfaces* **2018**, *10*, 10022.
[32] R. Thangavel, A. G. Kannan, R. Ponraj, G. Yoon, V. Aravindan, D.-W. Kim, K. Kang, W.-S. Yoon, Y.-S. Lee, *Energy Storage Mater.* **2020**, *25*, 702.
[33] J.-Z. Guo, P.-F. Wang, X.-L. Wu, X.-H. Zhang, Q. Yan, H. Chen, J.-P. Zhang, Y.-G. Guo, *Adv. Mater.* **2017**, *29*, 1701968.
[34] D. Wu, X. Li, B. Xu, N. Twu, L. Liu, G. Ceder, *Energy Environ. Sci.* **2015**, *8*, 195.
[35] Y. Jiang, X. Zhou, D. Li, X. Cheng, F. Liu, Y. Yu, *Adv. Energy Mater.* **2018**, *8*, 1800068.
[36] Z. Yang, G. Li, J. Sun, L. Xie, Y. Jiang, Y. Huang, S. Chen, *Energy Storage Mater.* **2020**, *25*, 724.
[37] L. Wu, Y. Hao, S. Shi, X. Zhang, H. Li, Y. Sui, L. Yang, S. Zhong, *Front. Chem.* **2018**, *6*, 616.
[38] W. Oh, H. Park, B.-S. Jin, R. Thangavel, W.-S. Yoon, *J. Mater. Chem. A* **2020**, *8*, 10331.
[39] J.-S. Park, J. Kim, J. H. Jo, S.-T. Myung, *J. Mater. Chem. A* **2018**, *6*, 16627.
[40] C. Wei, F. Luo, C. Zhang, H. Gao, J. Niu, W. Ma, Y. Bai, Z. Zhang, *Ionics* **2020**, *26*, 2343.
[41] A. N. Mansour, P. H. Smith, W. M. Baker, M. Balasubramanian, J. McBreen, *Electrochim. Acta* **2002**, *47*, 3151.
[42] S. Kim, Z. Zhang, S. Wang, L. Yang, E. J. Cairns, J. E. Penner-Hahn, A. Deb, *J. Phys. Chem. C* **2016**, *120*, 7005.
[43] W. H. Smyrl, S. Passerini, M. Giorgetti, F. Coustier, M. M. Fay, B. B. Owens, *J. Power Sources* **2001**, *97-98*, 469.
[44] O. Ojelere, D. Graf, T. Ludwig, N. Vogt, A. Klein, S. Mathur, *Dalton Trans.* **2018**, *47*, 6842.
[45] K. Ngamsai, A. Arpornwichanop, *J. Power Sources* **2015**, *295*, 292.
[46] R. Thangavel, K. Kaliyappan, K. Kang, X. Sun, Y.-S. Lee, *Adv. Energy Mater.* **2016**, *6*, 1502199.
[47] Y. Chen, Y. Xu, X. Sun, B. Zhang, S. He, C. Wang, *J. Power Sources* **2018**, *397*, 307.
[48] R. Klee, P. Lavela, M. J. Aragón, R. Alcántara, J. L. Tirado, *J. Power Sources* **2016**, *313*, 73.
[49] G. Silversmit, D. Depla, H. Poelman, G. B. Marin, R. De Gryse, *J. Electron Spectrosc. Relat. Phenom.* **2004**, *135*, 167.